Contents lists available at ScienceDirect

International Journal of Heat and Mass Transfer

3-D numerical study of subcooled flow boiling in a horizontal rectangular mini-channel by VOSET

Yu-Jie Chen[a], Kong Ling[a], Hao Ding[a], Yun Wang[b], Shu-Qi Jin[a], Wen-Quan Tao[a,*]

[a] Key Laboratory of Thermo-Fluid Science and Engineering, Ministry of Education, School of Energy & Power Engineering, Xi'an Jiaotong University, Shaanxi 710049, China
[b] CNNC Key Laboratory on Nuclear Reactor Thermal Hydraulics Technology, Nuclear Power Institute of China, Chengdu 610041, PR China

ARTICLE INFO

ABSTRACT

A three-dimensional conjugated numerical simulation is conducted to investigate subcooled flow boiling in a horizontal rectangular mini-channel based on the interface capturing method (VOSET). A reasonable nucleation density site model based on experimental results is adopted. Hundreds of bubbles with different sizes are successfully captured. Simulation results reproduce typical processes of subcooled boiling flow: growth, coalescence, detachment, and condensation of bubbles. And different flow boiling patterns, including pseudo bubbly flow, bubbly flow, slug flow, and pattern transition, are visualized under different heat fluxes. Furthermore, the effects of heat flux and vapor fraction on heat transfer coefficient are discussed in detail. Heat transfer deterioration is observed for high heat flux because of the formation of dry patches, and the complexity of heat transfer performance varying with vapor fraction is found. Based on those, the heat transfer mechanisms of subcooled flow boiling at different heat flux in the present mini-channel are discussed.

© 2021 Elsevier Ltd. All rights reserved.

1. Introduction

The heat transfer of two-phase flow boiling in mini-/microchannel, compared with single-phase flow heat transfer, is significantly enhanced at the same pumping power [1]. Therefore, two-phase flow boiling in the mini-/micro-channel has broad applications, including chip cooling in computer data centers [2], avionics cooling [3], satellite electronics cooling [4], advanced electronic equipment cooling [5], and cooling of electric vehicle IGBT power module [6]. Whereas some problems, such as instabilities of temperature and pressure, threaten the development and application of mini-/micro-channel flow boiling in practice. Moreover, the heat transfer mechanism of the two-phase flow boiling needs to be further revealed. Therefore, it is urgent to do more researches to meet the growing requirement of this type of heat transfer.

The mechanism of flow boiling heat transfer in the macro channel is different from that in mini-/micro-channel, and some classifications have been proposed to distinguish macroscopic channel and microcosmic channel [7–9]. However, there is no consensus on these classifications. A simple and commonly accepted classification for two-phase channel flow is to take a hydraulic diameter of 3 mm as the dividing size [1,8]. Channels with dimensions less

than 3 mm are classified as mini channels; channels with the dimension below 1 mm are regarded as microchannels; those above 3 mm are called conventional channels. This classification is also adopted in the present study. For the researches of flow boiling in the mini-channel, the heat transfer mechanism and effect factors like mass flux, heat flux, nanofluid, channel dimension, vapor quality, and fluid properties on heat transfer coefficient (HTC) are the focuses in the past decades. Following is a brief review of previous studies in this regard.

Qu and Mudawar [10] experimentally studied the saturated flow boiling heat transfer of water in a rectangular micro-channel heat sink with 21 parallel channels. Results indicated that HTC in the mini-channel heat sink was closely related to mass velocity but not to heat flux, and the dominant heat transfer mechanism was forced convective boiling. Lee and Mudawar [11] conducted experimental studies of subcooled flow boiling of HFE 7100 in a micro-channel heat sink with a channel width from 84.2 to 205 μm. It was found that critical heat flux (CHF) occurred at low mass velocities due to the vapor backflow to the inlet plenum, and the heat transfer instability could be weakened by decreasing the coolant temperature. Furthermore, the pressure drop in the micro-channel heat sink was analyzed [12]. Results indicated that pressure drop increased after bubble detachment from the wall and decreased with the increasing liquid subcooling. Mathew et al. [13] explored the two-phase cooling performance of water in a hybrid microchannel-microgap heat sink with a micro-gap of 0.6 mm

---

* Corresponding author.
E-mail address: wqtao@mail.xjtu.edu.cn (W.-Q. Tao).

(height) × 25 mm (width). A stable annular flow pattern in the microchannel was established at moderate to high heat flux, and thin-film evaporation resulted in an increased heat transfer coefficient in the channel downstream. Compared with the straight microchannel heat sink, the heat transfer performance of the hybrid heat sink was inferior. Bao et al. [14] revealed flow boiling heat transfer characteristics of Freon R-11 and HCFC123 in a 1.95 mm copper tube under the heat fluxes 5–200 kW/m². They found that vapor quality slightly affected HTC, while HTC significantly increased with the increasing heat flux. This implied that nucleate boiling was the dominant heat transfer mechanism in their study. Differently, Huo et al. [15] found that the HTC was dependent on vapor quality, and it increased to a platform first and then decreased with the increasing vapor quality. Similar experimental phenomena were found by Yan and Lin [16] and Lin et al. [17]. Tibirica and Ribatski [18] investigated the effects of mass flux, heat flux, saturated temperature, and vapor quality on HTC of R134a and R245fa flow boiling in a horizontal 2.3 mm tube. Results indicated that high heat flux, saturation temperature, and mass flux favored enhancing the heat transfer, and increasing vapor quality led to various heat transfer behaviors. Saitoh et al. [19] experimentally studied the flow boiling heat transfer of refrigerant R-134a in horizontal mini-tubes with three different inner diameters. Results showed that local HTC decreased with the increasing vapor quality once it exceeded some values, and the turning point for small tube diameter was earlier. Beside, the effect of mass flux on the local HTC decreased with decreasing tube diameter, but the impact of heat flux was strong in all three tubes. Li and Xu [20] investigated the flow boiling heat transfer of nanofluid in a single microchannel. Al_2O_3 nanoparticles with a size of 40 nm at a weight concentration of 0.2% were added to water. Results showed that nanofluids significantly mitigated the flow instability without the nanoparticle deposition effect. Moreover, nanofluid inhibited the dry patch development on the heating wall, leading to heat transfer enhancement.

In the above experimental studies, there are some differences in the effects of vapor quality, mass flux, and heat flux on HTC. The review of Cheng and Xia [1] also mentioned that the experimental data from the different independent studies showed somewhat different heat transfer trends at similar test conditions. In the experimental studies of flow boiling in mini-/micro-channel, the attainable information is limited because of measurement difficulties, leading to some deficiencies in understanding the flow boiling heat transfer mechanism in depth.

Numerical simulation method is a powerful tool to investigate flow boiling heat transfer in the mini-/micro-channel, by which the temperature, pressure, vapor fraction, and velocity distributions can be easily obtained and analyzed. The numerical simulation of flow boiling in mini-/micro-channel is challenging in accurate interface capture, nucleation modeling, etc. Many valuable studies have been reported, and different numerical models for flow boiling studies have been adopted in the literature. Soleimani et al. [21] compared simulation results of five common numerical models for flow boiling, including Volume of Fluid (VOF), Eulerian boiling, Eulerian Lee, Eulerian thermal phase change, and mixture models, with experimental results. Based on the comparisons of flow regime and heat transfer, the interface capture method VOF was recommended as the best model to simulate flow boiling in mini-channel at their simulation parameters. Beside, the interface capture method Level-set is also popular in flow boiling studies [22]. Among different numerical methods for interface capture, VOF [23] and Level-set [22] methods were proposed the earliest. In VOF method, a function for the reference phase (vapor phase for boiling) called volume fraction is used to indicate its fraction in a control volume, and it is advanced by solving a transient partial differential equation. In the Level-set method, a function (level

set function) is defined, of which the zero value is the indication of the interface of two phases, and it is also advanced by solving a transient partial differential equation. However, VOF and Level-set methods have their own shortcomings, and their advantages and disadvantages complement each other. Hence, some coupling VOF and Level-set methods were then proposed, such as CLSVOF [24]. But the computational efficiency of CLSVOF is inferior to the previous two methods. Later, VOSET was proposed in [25], and subsequent extension to 3D was conducted in [26]. In VOSET, both volume fraction and level set function are used, but only the volume fraction is advanced by solving the transient partial differential equation, while the level set function is determined by the geometric method. Hence, the computational time is greatly saved. However, to the author's knowledge, the applications of VOSET in the numerical simulation of in-tube boiling heat transfer are quite limited [27].

In the simulation of boiling heat transfer by the interface capture methods mentioned above, the determination of nucleation sites is an important issue. The nucleation process is hard to simulate by the macroscopic numerical simulation methods because of the scale limitation. This process is essentially at the scale of molecules. In the macroscopic numerical simulation, the practice of selecting an artificial bubble nucleus is usually adopted. Mukherjee and Kandlikar [28,29] numerically analyzed the growth of an artificially placed single vapor bubble in a microchannel by Level-set method. The initially placed bubble grew up with time, and finally, a vapor patch formed at the walls when the bubble filled the channel. Lee and Son [30] numerically studied a single bubble growth in a mini-channel using the Level-set method. An initial bubble was put on the bottom wall surface. Results indicated that HTC increased as the advancing and receding contact angles decreased. Zu et al. [31] used a vapor inlet to generate a pseudo bubble to study bubbly flow in a confined mini-channel using the VOF method. Thome and Magnini [32] put a bubble generation source at the upstream initial adiabatic section of the channel with a prescribed frequency. It was found that HTC significantly depended on the thickness of liquid film between bubble and wall. By using a local vapor inlet condition, Luo et al. [33] revealed the hydrodynamics and heat transfer performance of annular flow boiling in a rectangular microchannel. In the study of Ling et al. [27], VOSET method was employed to investigate the 2D subcooled flow boiling with some predetermined nucleation sites. In their study, the conjugated heat transfer between solid and fluid was considered, and a depletable microlayer model was utilized to describe the evaporation of microlayer. In some papers [34–37], the flow boiling studies in the mini-/micro-channel were conducted by software without providing the details of bubble generation.

The studies of flow boiling in the mini-/micro-channel are often conducted for the 2D model because of the computational cost. Zhuan and Wang [34] explored the boiling flow patterns of R-134a and R-22 in a 2D micro-channel. It was found that bubble growth and coalescence were significant for flow pattern transition. Huang et al. [35] conducted a 2D flow boiling numerical simulation of R141b in a mini-channel. Results indicated that the mini-channel size had a great impact on flow pattern and heat transfer performance, but heat flux, inlet velocity, and liquid subcool had a slight effect on HTC under their study conditions. Prajapati et al. [36] numerically investigated subcooled flow boiling in a segmented finned microchannel divided into the main and secondary channels. Results showed that the secondary channel weakened the bubble expansion and avoided channel blocking, enhancing the heat transfer. The generation and evolution of dry patches or vapor columns may cause heat transfer instability for flow boiling in the mini-/micro-channel, while the 2D numerical simulation method cannot describe those. Recently, a 3D numerical investigation was published by Hedau et al. [37]. It was found that the va-
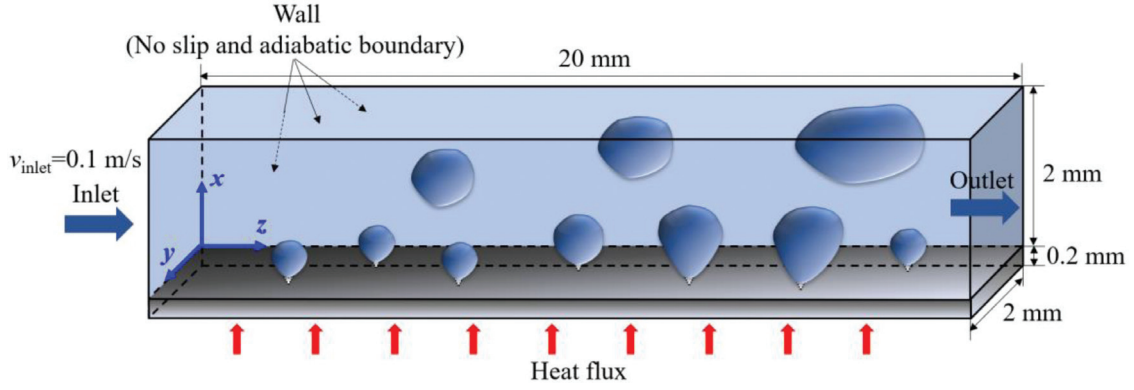
Fig. 1. configurations of 3D rectangular mini-channel.

Table 1
Physical properties of study mediums.

	Density (kg/m^3)	Viscosity (Pa·s)	Thermal conductivity (W/(m·K))	Heat capacity (J/(kg·K))
Wall	2330	–	148	766
Liquid	888.1	1.51×10^{-4}	0.674	4400
Vapor	5.14	1.5×10^{-5}	0.036	2712

por blocking in the channel near the outlet caused the instabilities in pressure drop, surface temperature, and mass flux.

The above researches have provided significant insights into the flow boiling in the mini-channel. However, the following aspects still need to be further studied. First, the bubble nuclei are often artificially selected, which hinders the study of heat flux effects. Second, most studies are of the 2D type, which cannot appropriately predict the dry patch and critical heat flux. In the present study, based on the nucleation density site model obtaining by the experimental method, the efficient method of VOSET is adopted to study the subcooled flow boiling in a 3D mini-channel by considering the conjugated heat transfer. And the bubble activities, flow pattern, and heat transfer of the subcooled flow boiling are investigated in detail under different heat fluxes.

2. Problem description

As shown in Fig. 1, the study subject is the subcooled flow boiling in a 3D horizontal rectangular mini-channel with a size of 2.0 mm (x) × 2.0 mm (y) × 20.0 mm (z). A solid wall consisting of monocrystal silicon with a size of 0.2 mm (x) × 2.0 mm (y) × 20.0 mm (z) is put on the bottom of the channel to conduct heat from heat source to liquid. The other three sides are smooth walls. Water flows from the left inlet to the right outlet with an inlet subcooling of 20 K ($\Delta T_{sub} = T_{sat} - T_{inlet}$) at 0.1 m/s.

The liquid pressure is 1 MPa, and the corresponding saturated temperature and latent heat of water are 453 K and 2.02×10^6 J/kg, respectively. Liquid-vapor surface tension is 0.042 N/m. The other physical properties are listed in Table 1. The heat fluxes applied to the bottom surface of the wall vary in the range of 100–500 kW/m^2. The bottom wall is hydrophilic with a contact angle of 50°.

3. Numerical models and verification

In this section, the models for describing the subcooled flow boiling in the mini-channel are illustrated, and the corresponding verifications are made.

3.1. Governing equations

As shown in Fig. 1, the computation region includes solid region and fluid region. The unsteady heat conduction in the solid region is described by Eq. (1).

$$\frac{\partial(\rho_s c_s T)}{\partial t} = \nabla \cdot (\lambda_s \nabla T) \tag{1}$$

where ρ is the density, kg/m^3; c is the heat capacity, J/(kg·K); λ is the thermal conductivity, W/(m·K).

The compression of fluid is not taken into account in the present study. Moreover, the liquid-vapor interface temperature is set as the saturated temperature, and it serves as the constant temperature of the interface boundary. Therefore, the heat transfer and convection in the fluid region can be described by Eqs. (2)–(5).

$$\nabla \cdot u = \left(\frac{1}{\rho_v} - \frac{1}{\rho_l}\right)\dot{m} \tag{2}$$

$$\frac{\partial(\rho u)}{\partial t} + \nabla \cdot (\rho u u) = -\nabla p + \nabla \cdot \left[(\eta + \eta_t)\left(\nabla u + \nabla u^T\right)\right] + f + \rho g \tag{3}$$

$$\frac{\partial\left(\rho_l c_{p,l} T\right)}{\partial t} + \nabla \cdot \left(\rho c_{p,l} u T\right) = \nabla \cdot (\lambda_l \nabla T) \tag{4}$$

$$\frac{\partial\left(\rho_v c_{p,v} T\right)}{\partial t} + \nabla \cdot (\rho c_{p,v} u T) = \nabla \cdot (\lambda_v \nabla T) \tag{5}$$

where $\dot{m}$ is the phase change rate, kg/(m^3·s); η is the dynamic viscosity, Pa·s; η_t is turbulent viscosity and is calculated by Smagorinsky model [38], Pa·s; f is the surface tension and is calculated by CSF model [39], N/m^3; g is gravity, m/s^2; indexes s, l, and v represent solid, liquid, and vapor, respectively. The phase change rate $\dot{m}$ is calculated by Eq. (6),

$$\int_V \dot{m} dV = \frac{1}{h} \int_A \dot{q} dA \tag{6}$$

where h is the latent heat of water, and the interface heat flux $\dot{q}$ is determined by Eq. (7).

$$\dot{q} = \lambda_v \left.\frac{\partial T}{\partial n}\right|_v - \lambda_l \left.\frac{\partial T}{\partial n}\right|_l \tag{7}$$

In the present study, the VOSET method is adopted to capture the vapor-liquid interface [25]. In the VOSET method, firstly, the VOF equation (Eq. (8)) is solved to obtain the volume fraction of liquid; then, the nearest distance from each mesh node to the vapor-liquid interface (Level-set function) is calculated by a simple

geometric method. The details of the 3D VOSET method can refer to Ref. [26].

$$\frac{\partial C}{\partial t} + \nabla \cdot (Cu) = -\frac{\dot{m}}{\rho_l} \qquad (8)$$

The discretization schemes for the transient term, convection term, and diffusion term of momentum and energy equations are first-order forward difference, MUSCL, and central difference, respectively. Beside, several time step limitations are made to improve numerical stability in the present study, and these limitations Eqs. (9)–((12)) refer to Ref. [40]. Generally, the time step is less than 1.0×10^{-6} s during the simulation process.

$$\Delta t \leq 0.8 \frac{\rho_v \Delta x^2}{6\eta_v} \qquad (9)$$

$$\Delta t \leq 0.8 \frac{\rho_l \Delta x^2}{6\eta_l} \qquad (10)$$

$$\Delta t \leq 0.5 \sqrt{\frac{(\rho_l + \rho_v)\Delta x^3}{\pi \sigma}} \qquad (11)$$

$$\Delta t \leq 0.1 \frac{\Delta x}{|u|_{\max}} \qquad (12)$$

where Δx is space step; σ is liquid-vapor surface tension coefficient; $|u|_{\max}$ is the maximum velocity.

The flow and thermal boundary conditions of the computational domain are set as follows. The constant temperature and velocity boundaries are applied at the inlet; the free outlet boundary is used at the outlet; the no-slip boundary is adopted for the velocity at all walls; the thermal boundary condition of constant heat flux is applied to the bottom surface of the channel, and all the other walls are adiabatic boundary. The so-called free outlet boundary condition can be regarded as no further change assumption, which is a convenient approximation for treating boundary conditions at the domain outlet. It has been widely adopted in Refs. [40–42] for in-tube boiling heat transfer simulation.

Come here to discuss an important issue: whether a microlayer is formed on the surface of heating wall at the present simulation condition. Urbano et al. [43] proposed the following discriminant.

$$\frac{Ja \cdot Ca}{(\theta - \theta_0)^3} > \frac{1}{A^3} \qquad (13)$$

where $\theta_0 = 5$ and $A = 313$; θ is the contact angle, °; the dimensionless numbers Ja and Ca are calculated by Eqs. (14) and (15).

$$Ja = \frac{\rho_l c_{p,l} (T_w - T_{sat})}{\rho_v h} \qquad (14)$$

$$Ca = \frac{v_{int} \eta_l}{\sigma} \qquad (15)$$

where $v_{int} \approx \frac{q_w}{\rho_v h}$ represents an indicator of the bubble growth velocity.

Based on the known physical properties in the present study, according to Eq. (13), the required superheat ($\Delta T_{sup} = T_w - T_{sat}$) for forming a micro-layer at the heat flux of 500 kW/m^2 should be equal to or larger than 45.8 K, which is much larger than the obtained superheat in this study. Therefore, no micro-layer will appear under the present simulation conditions, and it will not be considered in the present study.

3.2. Nucleation density site model

The locations and conditions of bubble nucleation should be given in the numerical simulation of the flow boiling heat transfer by the interface capture method. Numerical simulation of bubble
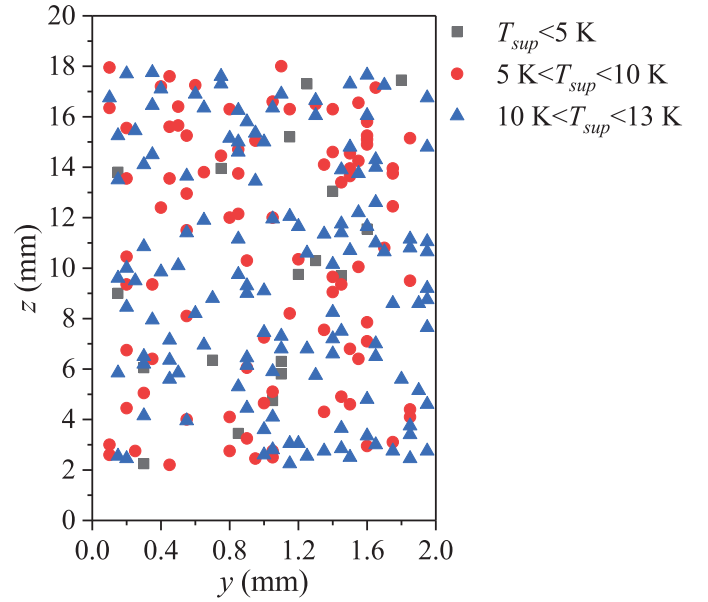
Fig. 2. Diagrammatic sketch of nucleation sites distribution (For interpretation of the references to color in this figure, the reader is referred to the web version of this article).

nucleation usually adopts the molecular dynamics method or/and lattice Boltzmann method. In this paper, a nucleation density site model from experimental study will be used. When the node on the wall surface satisfies the nucleation condition, an initial bubble nucleus with a diameter of 50 μm is artificially put on there. Therefore, the key is to obtain reasonable active nucleation site density under specific conditions.

After a literature search, the model developed by Li et al. [44] is adopted to determine the active nucleation site density. This model is shown in Eqs. (16)–(20), where the active nucleation site density is related to the pressure, wall superheat and contact angle. The model application scope is as follows: 0.101 MPa $\leq$ pressure $\leq$ 19.8 MPa, 5° $\leq$ contact angle $\leq$ 90°, 1.0×10^4 site/m$^2 \leq$ active nucleation site density $\leq 1.51 \times 10^{10}$ site/m^2.

$$N_w = N_0 (1 - \cos\theta) \exp\left[f(P)\right] \Delta T_{sup}^{A\Delta T_{sup}+B} \qquad (16)$$

$$f(P) = 26.006 - 3.678 \exp(-2P) - 21.907 \exp\left(-\frac{P}{24.065}\right) \qquad (17)$$

$$A = -0.0002P^2 + 0.0108P + 0.0119 \qquad (18)$$

$$B = 0.122P + 1.988 \qquad (19)$$

$$1 - \cos\theta = (1 - \cos\theta_0)\left(\frac{T_c - T_{sat}}{T_c - T_0}\right)^\gamma \qquad (20)$$

where $N_0 = 1000$ site/m^2, $\theta_0 = 41.37°$, $T_c = 374$ °C, $T_0 = 25$ °C, $\gamma = 0.719$ by default. The unit for pressure is MPa. Ref. [44] showed that the active nucleation site density predicted by this model is in good agreement with various published experimental data.

Among three parameters of this model, only the wall superheat changes as a parameter in this study. Therefore, the active nucleation site number is decided by the wall superheat. It is worth emphasizing that except for regions near the inlet and outlet of the mini-channel, the other substrate region is set as the nucleation region. The nucleation site is randomly placed on the mesh nodes of the nucleation region, as shown in Fig. 2. Different colors indicate different required superheat for activating the bubble nucleus. The nucleation sites with black and red colors are activated when
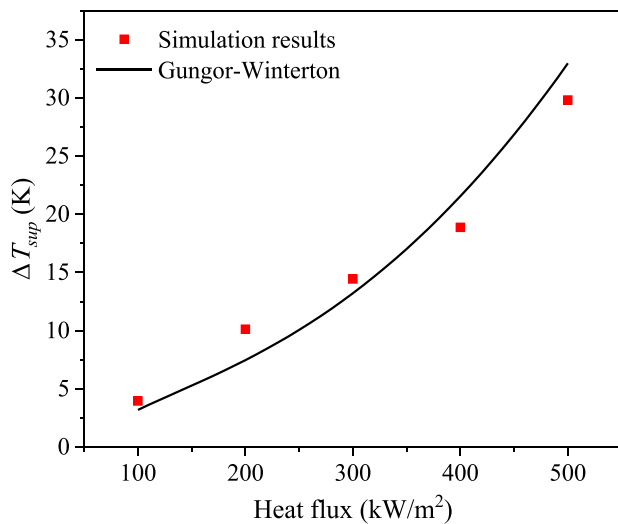
Fig. 3. Wall average superheat comparison between Gungor-Winterton equation and present simulation results under different heat fluxes.

the superheat exceeds 10 K. It is noteworthy that Fig. 2 is just a diagrammatic sketch. In the present study, new activated nucleation sites will be detected when the wall superheat increases 0.1 K every time.

3.3. Numerical methods and model verification

The above governing equations are numerically solved by the finite volume method with self-programming codes. The projection algorithm is adopted to deal with the coupling between pressure and velocity, and the algebraic multigrid method is used to solve the discretization equations efficiently. On the aspect of mesh, a fine grid spacing of 20 μm is applied to the x-direction of the solid region to guarantee the computational accuracy of heat conduction. For the fluid region, a comparison between the average wall superheat calculated by the mesh with uniform 640,000 nodes and 973,360 nodes is made under the heat flux of 300 kW/m^2. The fluid region and the solid wall region are solved integrally. Results show that the average wall superheats are 14.44 and 13.73 K for these two meshes, and the corresponding relative difference is 4.92%. This relative difference is acceptable considering the high computation cost and the complexity of the two-phase problem. Therefore, in the present study, a mesh with the total nodes of 800,000 (includes 160,000 nodes for the solid region) is employed to study the subcooled flow boiling in a mini-channel under different heat fluxes.

The equation proposed by Gungor and Winterton [45] based on experimental data for the subcooled flow boiling heat transfer is used to validate our numerically predicted results.

$$q = h_{sp,l}(T_w - T_b) + Sh_{nb}(T_w - T_{sat}) \qquad (21)$$

where $h_{sp,l}$ is the heat transfer coefficient of single-phase liquid and is calculated by Dittus–Boelter correlation [46] Eq. (22)), W/(m^2·K); T_b is liquid temperature, K; h_{nb} is the heat transfer coefficient of nucleate pool boiling and is calculated by Cooper equation [47] (Eq. (23)), W/(m^2·K); S is determined by Eqs. (24) and ((25).

$$h_{sp,l} = 0.023 \mathrm{Re}_l^{0.8} \mathrm{Pr}_l^{0.4} \frac{\lambda}{D} \qquad (22)$$

$$h_{nb} = 55 P_R^{0.12} (-0.4343 \ln P_R)^{-0.55} M^{-0.5} q^{0.67} \qquad (23)$$

$$S = 1 / \left(1 + 1.15 \times 10^{-6} F^2 \mathrm{Re}_l^{1.17}\right) \qquad (24)$$

$$F = 1 + 2.4 \times 10^4 Bo^{1.16} \qquad (25)$$

where P_R is the relative pressure on the critical pressure; M is the molecular mass, kg/kmol; $Bo = \frac{q}{Gh}$ is boiling number; G is mass flux, kg/m^2·s.

Fig. 3 illustrates the comparison of average wall superheat between Gungor-Winterton equation and present simulation results under different heat fluxes. Results indicate that the maximal relative difference is 35.4%, and the average relative difference is 17.9%. Qualitatively, the agreement in Fig. 3 is very good. Quantitatively, the discrepancy seems a bit large. Several possible causes are analyzed as follows. One is the effect of the length-to-diameter ratio (l/d) of the simulated tube. The Gungor-Winterton correlation was obtained from the test of a much larger l/d ratio. In addition, only one side of the tube is heated in our simulation, while experimental measurements were conducted with full-perimeter heating. However, it is well-known in the heat transfer textbook [46,48] that the Rohsenow equation for pool boiling heat transfer can be in error by 30% for a wall superheat by given heat flux. Therefore, the agreement of simulation results of the present study with the experimental equation can be considered acceptable.

Finally, some limitations of the present numerical simulation study are discussed. First, because of the computational cost, the length-to-diameter ratio of the present study is only ten. Such a short ratio with a uniform inlet velocity distribution assumption may affect the predicted flow pattern. Second, an initial bubble with a radius of 50 μm is put on the nucleation site. Thus the predicted results can only be applied for this case. Further study on the effects of the initial bubble size should be performed.

4. Results and discussion

In this section, the flow pattern, temperature, and velocity distribution, and HTC of the subcooled flow boiling in a 3D mini-channel with a square cross-section predicted by the self-programming codes are presented.

4.1. Flow pattern of subcooled flow boiling in a mini-channel under different heat fluxes

Firstly, the flow pattern under different heat fluxes is presented in this section because of its significant impact on the flow boiling heat transfer [34].

Figs. 4–9 illustrate the representative snapshots of 3D subcooled flow boiling in the mini-channel. The light blue, dark blue, and gray represent liquid water, vapor bubble, and solid wall, respectively. A dynamic equilibrium of heat exchange has been achieved at 500 ms, which will be illustrated in the next section. Therefore, these displayed snapshots in this section are within 500 ms. From the simulation results, different flow patterns of subcooled flow boiling, including pseudo bubbly flow, bubbly flow, slug flow, and pattern transition, are visualized under different heat fluxes. As shown in Fig. 4, at the heat flux of 100 W/m^2, only several isolated bubbles occur in the mini-channel within 500 ms, which is still the single-phase flow basically. The reason for this phenomenon includes three parts: the initial bubble does not grow up to a big one because of low wall superheat and high liquid subcooling; under the coupling effects of gravity, shear force, and surface tension, the small bubble detaches from the wall in a short time with a diameter below 0.2 mm, which is similar to the experimental results of Situ et al. [49]; it hard for these detached bubbles to coalesce into a big one because only a few nucleation sites are activated under low wall superheat. As a result, these small bubbles condense and disappear quickly in the subcooled liquid, and only pseudo bubbly flow happens in the mini-channel when the heat flux is 100 kW/m^2.
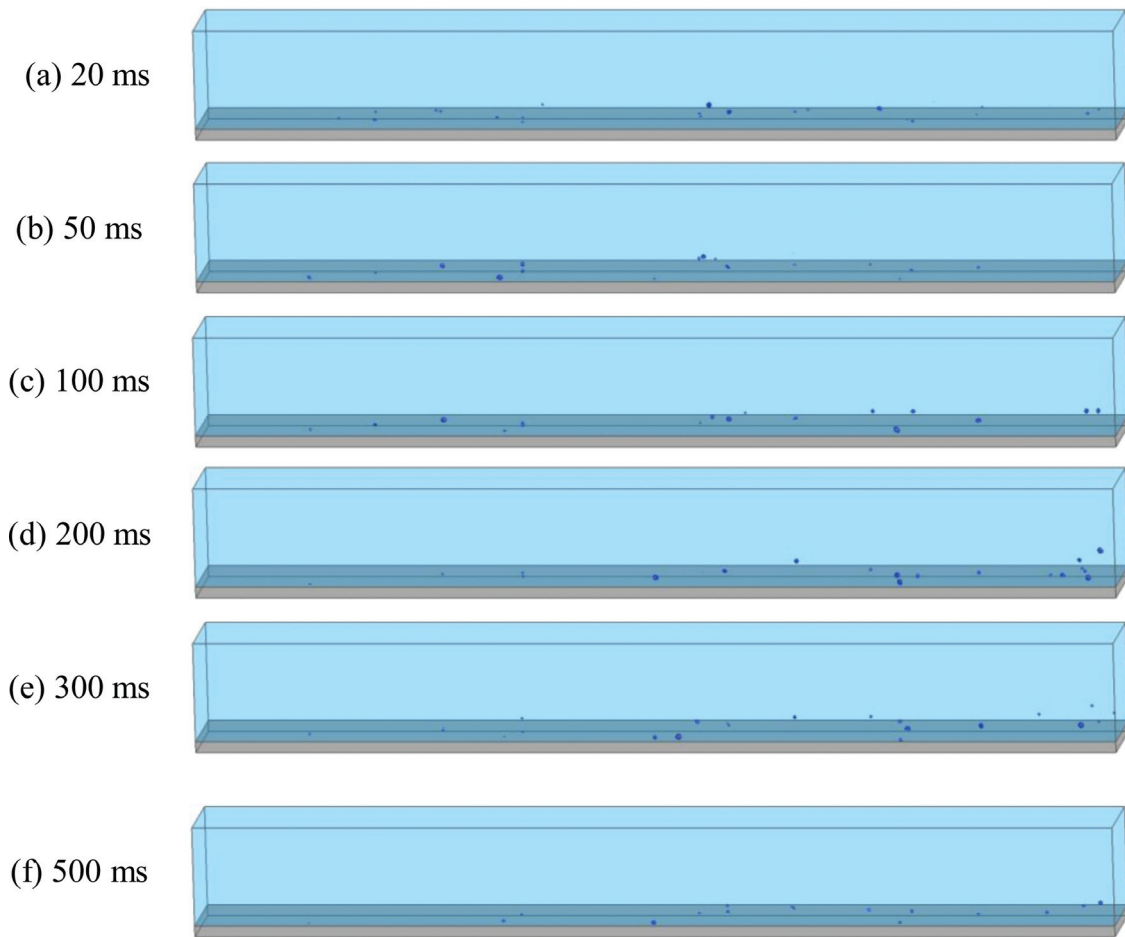
Fig. 4. Snapshots of 3D subcooled flow boiling with a heat flux of 100 kW/m². (For interpretation of the references to color in this figure, the reader is referred to the web version of this article).

Fig. 5 shows the representative snapshots for the case with a heat flux of 200 kW/m². More nucleation sites are activated with the increasing heat flux. Moreover, the detached diameter of the bubble becomes larger. Several bubbles coalesce into a big one, which is not easy to shrink and disappear inside the subcooled liquid, causing the increasing bubble diameter along the flow direction. Therefore, at this heat flux, a bubbly flow happens in the studied mini-channel. Beside, it is found that a quite bigger bubble occurs on the wall surface at a time of 500 ms, as shown in Fig. 5(f).

The bubbly flow also happens in the studied mini-channel when heat flux is equal to 300 kW/m², as shown in Fig. 6. The bubble size is still smaller than the channel height, but at the same time step, it is much larger than that inside the mini-channel with a heat flux of 200 kW/m². It is noteworthy that the shapes of the big bubbles are not spherical because of the liquid shear effect and bubble coalescence. On the other hand, some bubbles detach from the heating wall and move upward under the buoyancy effect. On the way to the top boundary, they condense and gradually become smaller inside the subcooled liquid, as shown in Fig. 7.

As the heat flux increases to 400 kW/m², a large number of nucleation sites are activated. As shown in Fig. 8, these activated bubbles grow up quickly and coalesce frequently. The bubble size significantly increases along the flow direction, and small bubbles

tend to coalesce with each other and form a bigger one. As a result, a single big bubble coalesced by several small bubbles appears near the outlet at 200 ms, and the mini-channel section is almost fully occupied. Even so, at this level of heat flux, no elongated bubble is found in the mini-channel.

When the heat flux is further raised to 500 kW/m², the elongated bubble appears in the second half of the mini-channel at about 200 ms, as shown in Fig. 9(d). High heat flux causes the quick generation of many big bubbles and makes the boiling very violent. The bubble size near the inlet of the channel with the heat flux of 500 kW/m² is even bigger than that near the outlet of the channel with a low heat flux (say, 200 kW/m²). Big bubbles keep coalescing with each other, but limited by the cross-section size of the mini-channel, and they extend along the z-direction, leading to the formation of elongated bubbles. Once the elongated bubble contacts the channel wall, a window may appear within this elongated bubble, as shown in Fig. 9(d). Beside, some liquids are blocked between two elongated bubbles, and the so-called slug flow happens, as shown in Fig. 9(e). In addition, when an elongated bubble is just formed, a thin film exists between the bubble and wall, as shown in Fig. 9(d). The high heat flux soon evaporates the thin liquid film, causing the appearance of a local dry patch, as witnessed in Fig. 9(f). The heat transfer deteriorates with the extending of the dry patch, which will be further discussed in the next section.
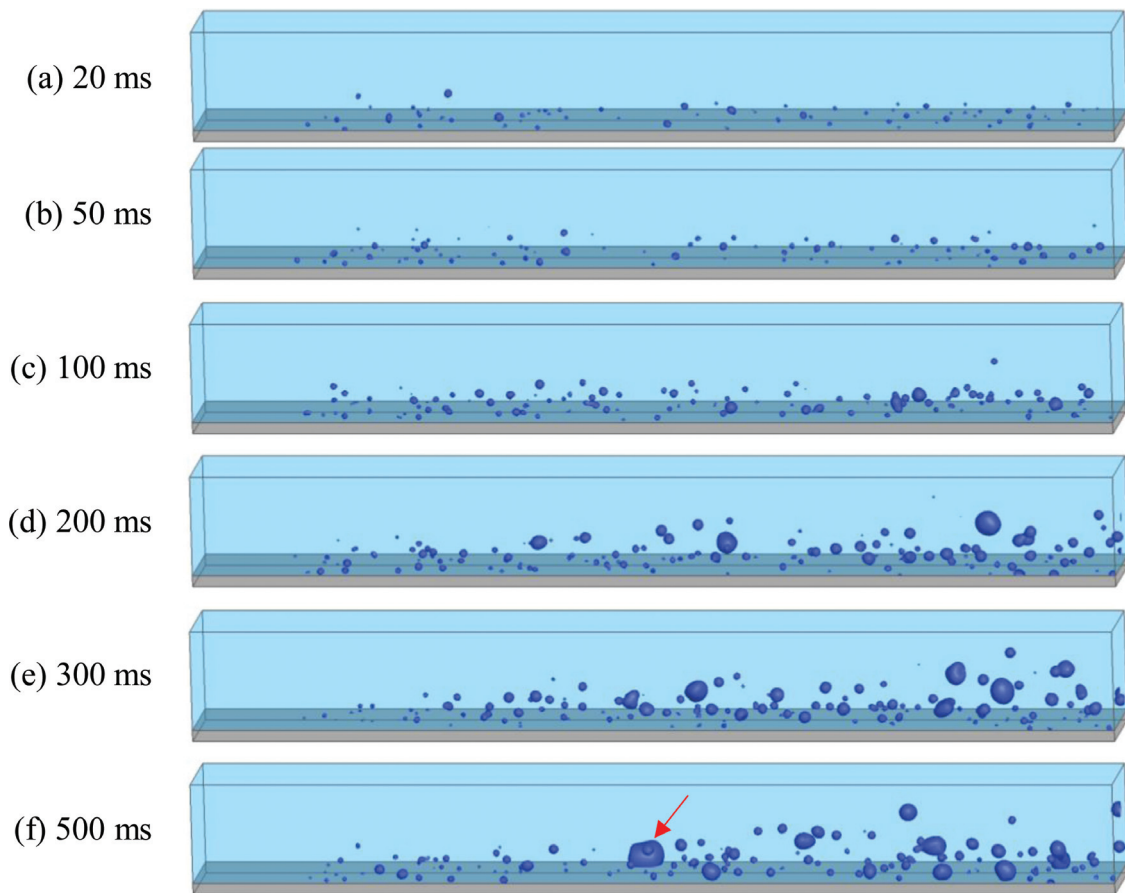
Fig. 5. Snapshots of 3D subcooled flow boiling with a heat flux of 200 kW/m². (For interpretation of the references to color in this figure, the reader is referred to the web version of this article.)

In summary, different heat fluxes cause significant differences in active nucleation site density, bubble growth, and coalescence. As a result, the pseudo bubbly flow, bubbly flow, slug flow, and the pattern transition between them are predicted successively in the mini-channel with the increasing heat flux. Beside, under high heat flux, a large number of nucleation sites are activated, and hundreds of bubbles are captured in the studied mini-channel. To our knowledge, similar numerical simulation of 3D cases based on the accurate interface capture method is very limited in the literature.

4.2. Heat transfer of subcooled flow boiling in a mini-channel under different heat fluxes

Nucleate boiling dominance and convection boiling dominance are two primary mechanisms of flow boiling heat transfer in a channel [1]. Quantitatively speaking, nucleate boiling dominance is related to bubble dynamics, and HTC depends on heat flux. Convection boiling dominance is related to liquid film evaporation, and HTC depends on mass flux and vapor quality. In this section, the flow boiling heat transfer in the mini-channel is discussed in detail based on these two flow boiling heat transfer mechanisms and flow patterns. It is worth stressing that the saturated liquid temperature is set as the reference temperature in the present study, and all displayed temperature information in the following parts is the excessive temperature.

4.2.1. Superheat of the heating wall surface under different heat fluxes

At each time step, the spatial average heating wall superheat is calculated to obtain its changing trends when different heat fluxes are applied to the bottom of the mini-channel. As shown in Fig. 10, the wall superheats rise first for all cases with different heat fluxes due to single-phase flow, and the rising amplitude increases with the increasing heat fluxes. And then, the change trends are different after the happening of flow boiling, but approximately stable wall superheats are obtained finally. The magnitudes of these approximately stable wall superheats for heat fluxes from 100 kW/m² to 500 kW/m² are 3.96, 10.12, 14.44, 18.88, and 29.82 K, respectively. When the heat flux is 100 kW/m², the wall superheat quickly decreases and reaches a stable value after about 500 ms. When heat flux equals 500 kW/m², the wall superheat reaches 23.31 K soon, and it increases once again because of the appearance of the local dry patch after about 150 ms, as shown as the turning point in Fig. 10. It is noteworthy that the wall superheats always fluctuate with time for all cases, and the amplitude increases with heat flux and reaches the maximum values at the heat flux of 500 kW/m². Therefore, the cases with the heat fluxes of 400 and 500 kW/m² are selected to illustrate the details of temperature distributions, including the wall superheat variation trends.

Fig. 11 shows temperature contours at the central section of y-direction and heating wall surface of mini-channel with a heat flux of 400 kW/m². It can be found that the wall superheat in the downstream region is evidently lower than that near the mini-channel inlet because of the cooling effect of nucleate boiling, while in the downstream of the central section, fluid temperatures are appreciably higher than the inlet because of the heating effect of the bottom wall. Fig. 12 shows the growth, movement, coalescence, and detachment of bubbles in the central section, which causes violent disturbance in the channel
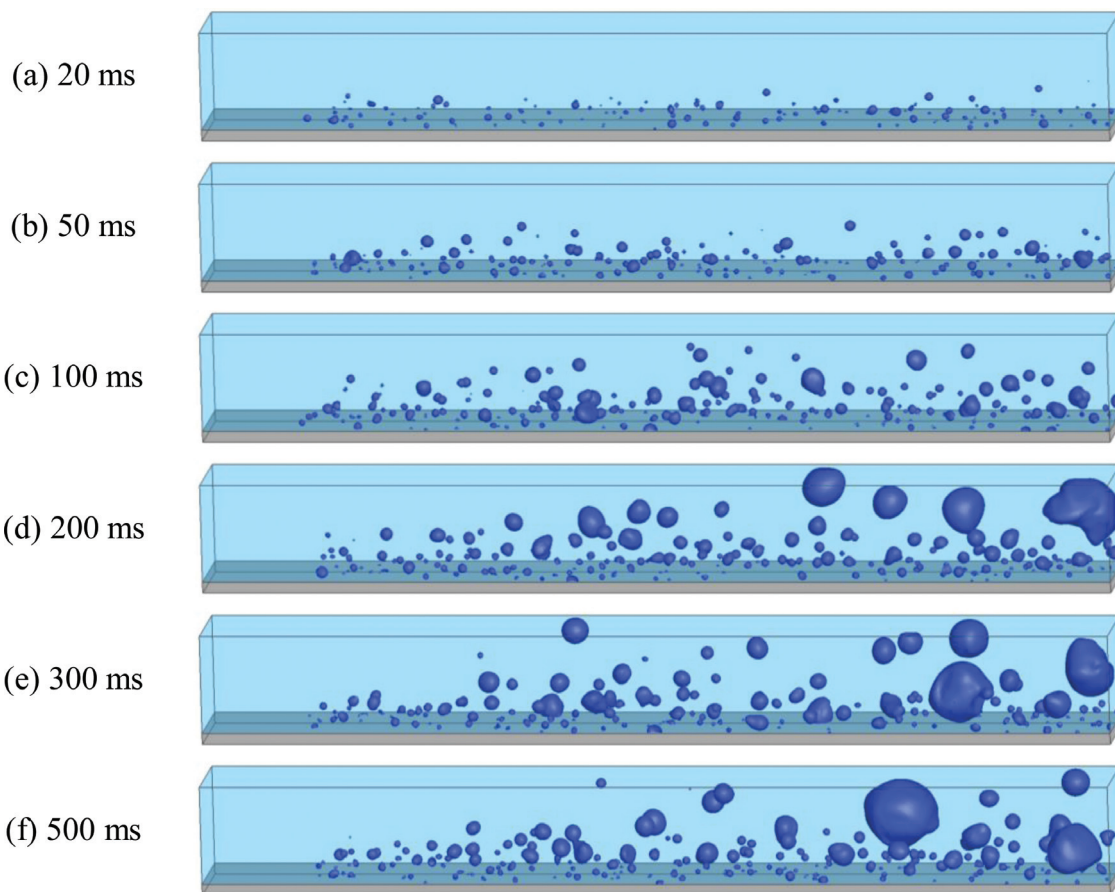
Fig. 6. Snapshots of 3D subcooled flow boiling with a heat flux of 300 kW/m². (For interpretation of the references to color in this figure, the reader is referred to the web version of this article.)
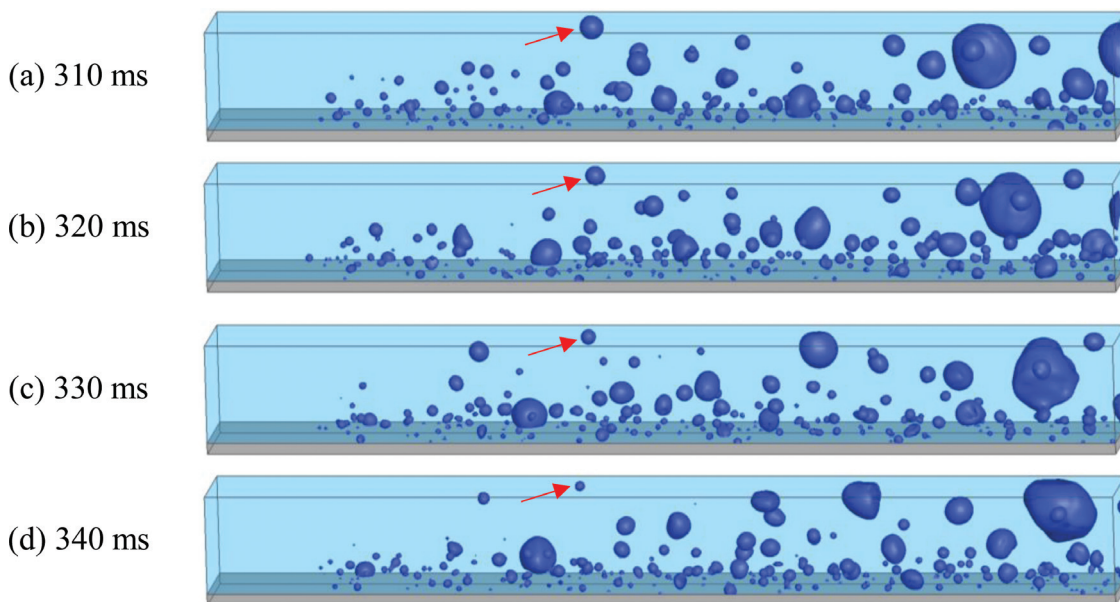
Fig. 7. Condensation of bubble inside the subcooled liquid. (For interpretation of the references to color in this figure, the reader is referred to the web version of this article.)
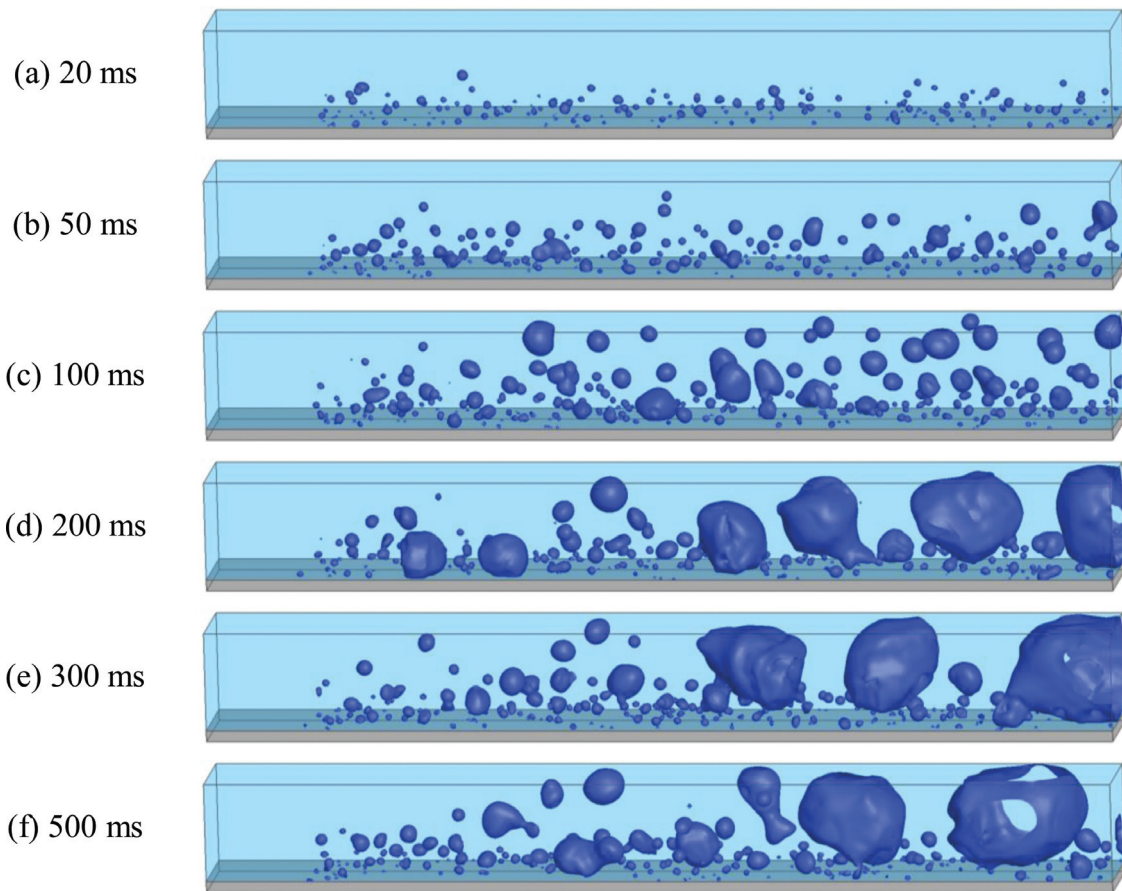
Fig. 8. Snapshots of 3D subcooled flow boiling with a heat flux of 400 kW/m². (For interpretation of the references to color in this figure, the reader is referred to the web version of this article.)

and enhances the cooling effect. Therefore, the wall superheat is lower in the central and downstream regions where flow boiling happens. When the cooling effects and constantly heating with a heat flux of 400 kW/m² reach a dynamic equilibrium, an approximately stable wall superheat is reached, as shown in Fig. 10.

Fig. 13 shows temperature contours at the central section of the *y*-direction and heating wall surface of the mini-channel with a heat flux of 500 kW/m². At 100 ms, the bubble size is smaller than the channel height, and the movement and growth of big bubbles make the wall superheat somewhat uniform at 100–150 ms. However, these big bubbles coalesce into a few elongated bubbles at about 150 ms and cause the formation of a dry patch on the heating wall surface, as shown in Fig. 13(b). The heat transfer in the dry patch begins to deteriorate, thus the wall superheat increases as indicated by the rising turning point in Fig. 10. More elongated bubbles are formed with time, and the dry patch area is growing, causing an increase in the local hot region area, as shown in Figs. 13(c) and (d). Moreover, with the movement of the elongated bubble along the flow direction, the dry patch changes its area and location, leading to the fluctuation of wall superheat with a relatively large amplitude. It is emphasized that the dry patch cannot be visualized by 2D numerical simulation, which is one of the reasons for the present 3D numerical study.

4.2.2. Average HTC of the heating wall under different heat fluxes

HTC is one of the most concerning parameters in flow boiling in the mini-channel and is also related to the heat transfer mech-

anism of flow boiling. Therefore, the relationships between HTC and heat flux are studied in this part. At each time step, the average liquid temperature and wall surface temperature are obtained to calculate the spatial average HTC of the wall. Then, the time-space average HTC of the heating wall is calculated by the following equation,

$$h_w = \sum_{t}^{t+\Delta t} \frac{q}{\left(T_{ave,w} - T_{ave,b}\right)} / \Delta t \qquad (26)$$

Fig. 14 illustrates the time-space average HTC of the heating wall under different heat fluxes. It is found that HTC increases first and then decreases with wall superheat appreciably, and HTC is related to the heat flux. Therefore, the dominant mechanism of subcooled flow boiling heat transfer in the present mini-channel is nucleate boiling. The HTC of single-phase flow at the present flow conditions predicted by Eq. (22) is 2204.3 W/(m²·K), which is much lower than that of the subcooling flow boiling. Moreover, the HTC increases with the heat flux till heat flux is equal to 400 kW/m² due to the enhancement of nucleate boiling intensity, as shown in Figs. 4–6, and 8. However, when heat flux is beyond 400 kW/m², the heat transfer is deteriorated because of the appearance of the local dry patch, as analyzed in the previous paragraph.

4.2.3. Local HTC and vapor fraction along flow direction under different heat fluxes

The local HTC and vapor fraction along flow direction under different heat fluxes are analyzed in this section. For this purpose,
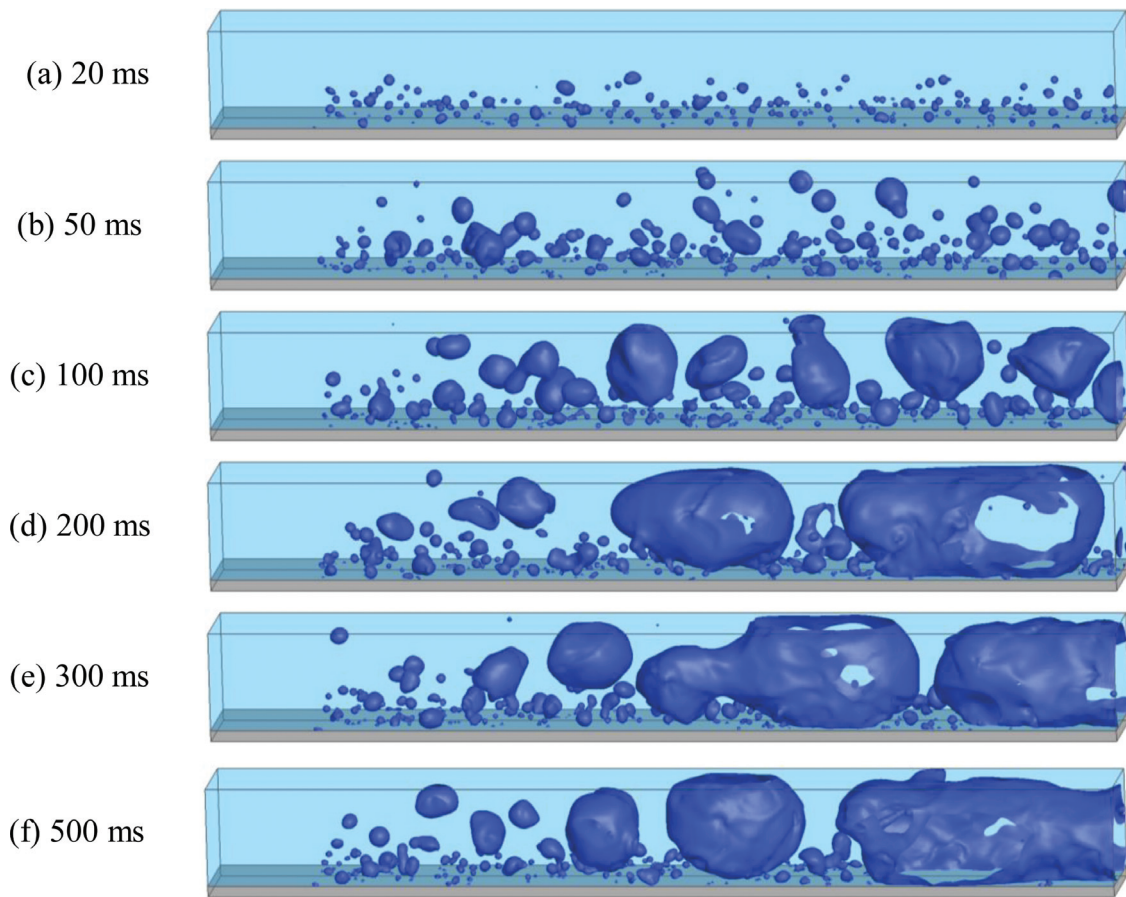
Fig. 9. Snapshots of 3D subcooled flow boiling with a heat flux of 500 kW/m^2. (For interpretation of the references to color in this figure, the reader is referred to the web version of this article.)
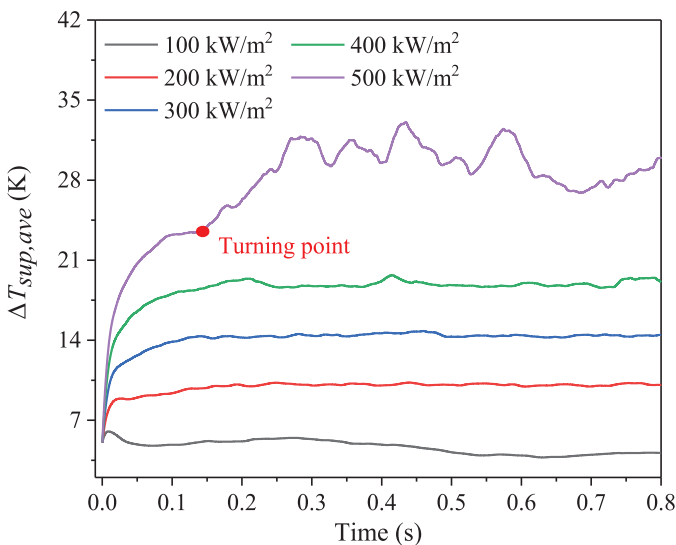
Fig. 10. Trends of spatial average heating wall superheats under different heat fluxes.

the mini-channel is uniformly divided into 20 subregions along the flow direction. The local HTC and vapor fraction of each subregion are calculated and averaged during the stable stage to explore their relationship. Figs. 15 and 16 show local vapor fraction

and HTC profiles along z-direction under different heat fluxes, respectively. Except for the cases with a heat flux of 100 kW/m^2, the vapor fraction in other cases increases with the flow direction, and the increment is small for the case with a heat flux of 200 kW/m^2. When the heat flux is low, a few nucleation sites are activated, and the detached bubble may disappear within the subcooled liquid in a short time. Therefore, the vapor fractions near 0 along the flow direction when the heat flux is 100 kW/m^2.

As shown in Fig. 16, the HTC profiles show different characteristics under different heat fluxes. When the heat flux is 100 kW/m^2, HTC changes slightly along the flow direction because few nucleation sites are activated. Even though the bubble activation is not violent, the HTC of this case still much higher than that of pure single-phase flow. As the heat flux is raised to 200 and 300 kW/m^2, HTC increases appreciably along the flow direction because of the heat transfer enhancement caused by the violent activities of bubbles. It is noteworthy that the heat transfer is evidently enhanced along the flow direction for the case with a heat flux of 200 kW/m^2, although the vapor fraction is at a low level. When the heat flux is 400 kW/m^2, the HTC increases first and then reaches a platform in the second half of the mini-channel, as shown in the region signed with two red dotted lines in Fig. 16. Furthermore, for the case with a heat flux of 500 kW/m^2, the local HTC decreases appreciably from the peak due to the formation of a dry patch.

Based on the above discussion of the HTC and vapor fraction profiles along the flow direction, some relationships between them are found for the studied mini-channel: (1) the HTC changes

(a) 100 ms

(b) 200 ms

(c) 300 ms
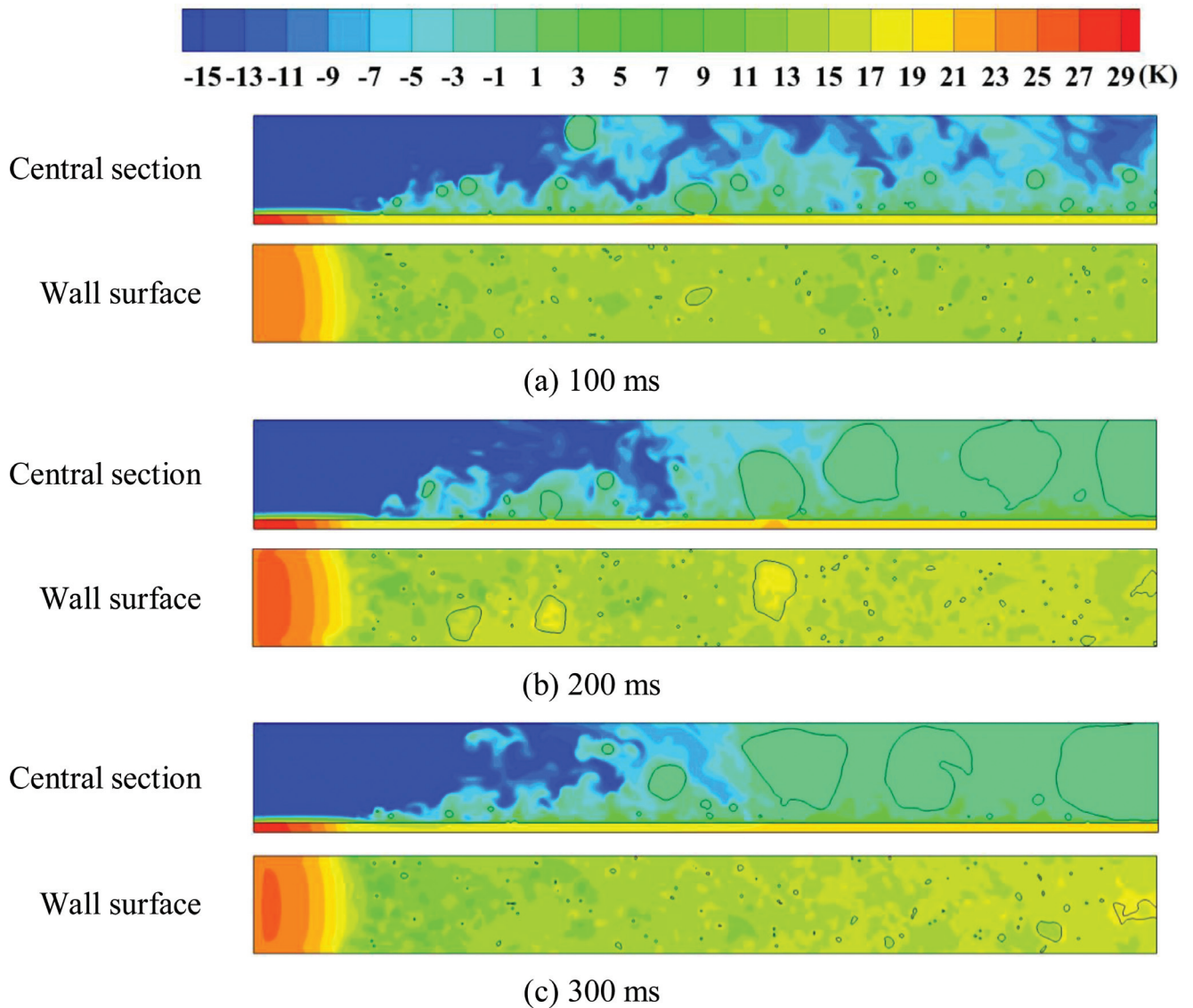
Fig. 11. Temperature contours at the central section and heating wall surface of the mini-channel with a heat flux of 400 kW/m^2.

slightly along the flow direction when the vapor fraction keeps at a very low level; (2) the HTC increases with the increasing vapor fraction along the flow direction when the vapor fraction is lower than 0.18; (3) HTC gets into a platform with a value between 19,500 and 21,000 W/(m^2·K) when the vapor fraction is in a range from 0.18 to 0.45; (4) the HTC monotonically decreases with the increasing vapor fraction when the vapor fraction is over 0.45. Qualitatively, these observations are similar to the experimental results of Huo et al. and Lin et al. [15,17]. Huo et al. [15] conducted

an experimental investigation of flow boiling of R134a in two tubes with diameters of 2.01 and 4.26 mm. Their results indicated that under different heat fluxes, the HTC increased with the increase of vapor fraction within 0.05; then, HTC almost stayed unchanged in the vapor fraction range from 0.05 to 0.2; finally, HTC monotonically decreased with the further increase of vapor fraction.

The reasons for relationships (1), (2), and (4) have been clarified by the above illustrations of Figs. 15 and 16. The reasons for relationship (3) can be explained by the snapshots of 3D subcooled

Fig. 12. Velocity distribution at the central section of the mini-channel with a heat flux of 400 kW/m^2 at 100 ms.

flow boiling in the mini-channel shown in Figs. 8 and 9. When the vapor fraction is in a range from 0.18 to 0.45, the flow pattern is the big bubble flow, and the positive effects of nucleate boiling on HTC have peaked in the confined mini-channel. On the other hand, there is no significant difference in the evaporation effect at the

interface of these big bubbles because the liquid film between the bubble and the heating wall is thick. Therefore, the HTC reaches a platform when the vapor fraction ranges from 0.18 to 0.45.

Obviously, HTC is also related to vapor fraction, and the convective effects should be considered for the heat transfer mechanism
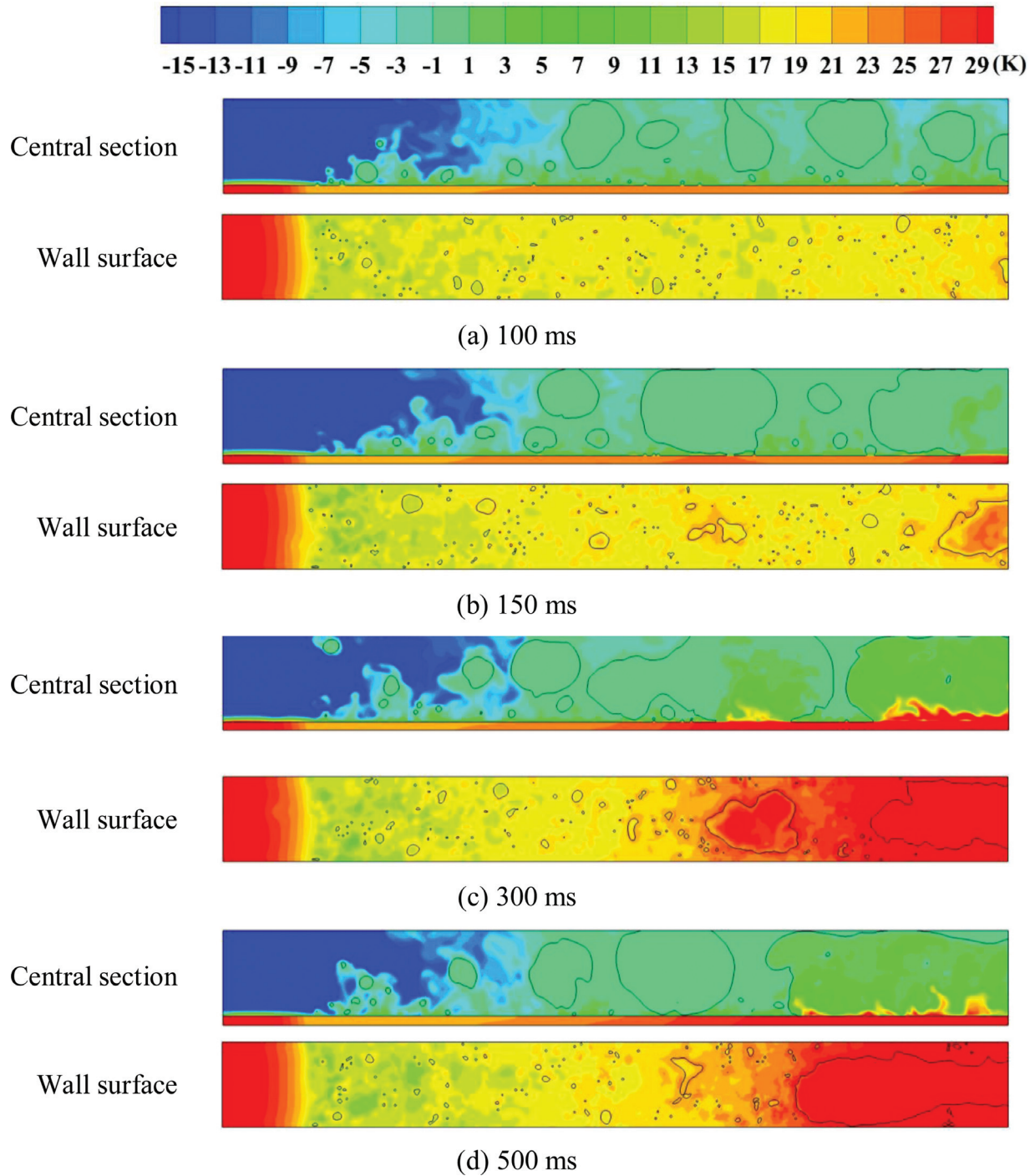
Fig. 13. Temperature contours at the central section and heating wall surface of the mini-channel with a heat flux of 500 kW/m^2.
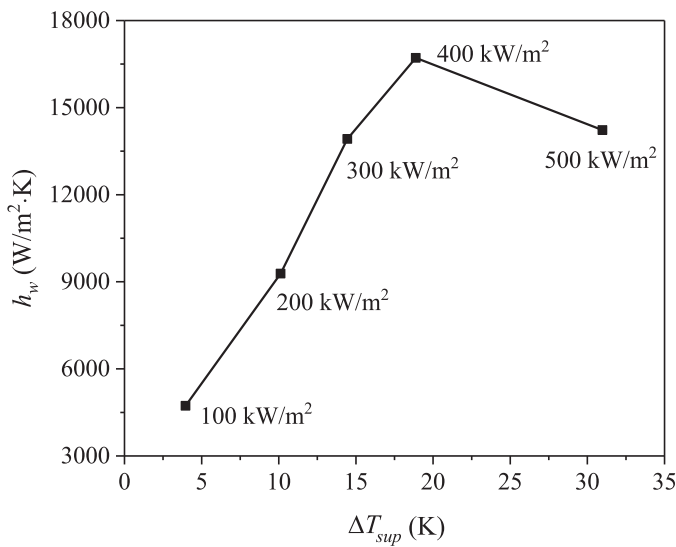
Fig. 14. Time-space average HTC of the heating wall under different heat fluxes.
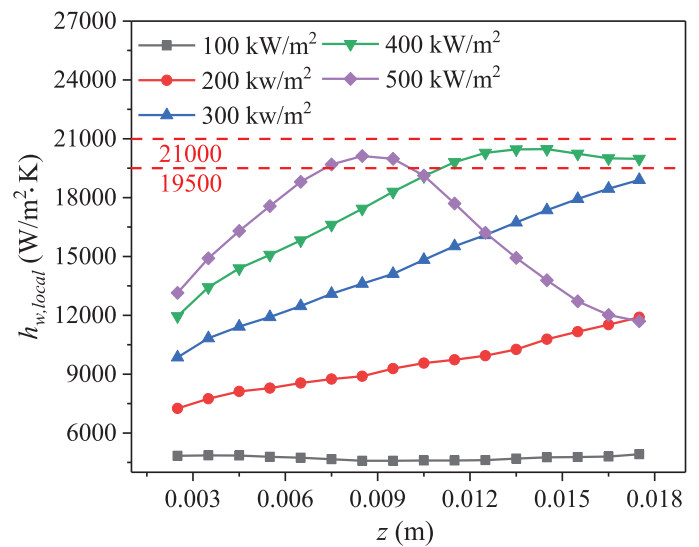
Fig. 16. HTC profiles along flow direction under different heat fluxes (For interpretation of the references to color in this figure, the reader is referred to the web version of this article).
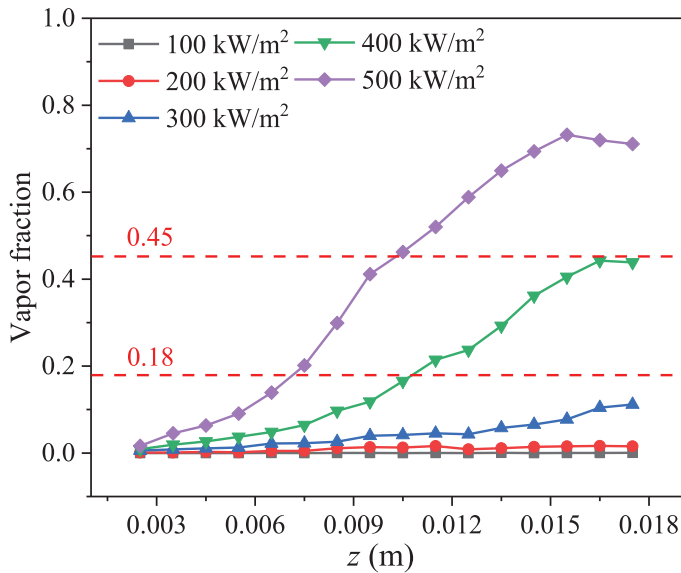
Fig. 15. Vapor fraction profiles along flow direction under different heat fluxes.
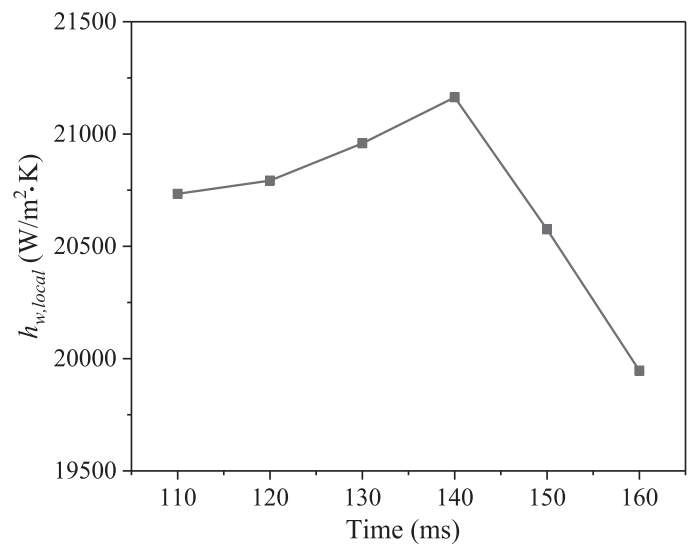
Fig. 17. Trend of spatial average HTC in the second half of the mini-channel.

in this study. The evaporation of elongated bubbles plays a vital role in the heat transfer mechanism of convective boiling dominance [1]. The elongated bubble forms in the second half of the mini-channel when the heat flux is 500 kW/m², and the region from 12 to 18 mm in the z-direction is chosen to calculate its spatial average HTC. Fig. 17 shows the trend of the spatial average HTC from 110 to 160 ms, which is the period of a dry patch formation. Results in Fig. 17 indicate that the HTC increases with time before the appearance of a dry patch (~140 ms). However, as shown in Fig. 18, bubble activities are gradually suppressed with the formation of the elongated bubble from 110 to 140 ms in the second

half of the mini-channel, and no dry patch forms in the wall surface before 140 ms. Therefore, the evaporation effect contributes to the heat transfer enhancement from 110 to 140 ms. On the other hand, the evaporation effect is obviously weaker than the nucleate boiling effect on the heat transfer enhancement by comparing the improvement range of local HTC in Figs. 16 and 17.

In summary, for the subcooled flow boiling in the present mini-channel, the nucleate boiling is the primary heat transfer mechanism at a vapor fraction below 0.45, and the convective effect contributes to the HTC at a high vapor fraction before the appearance of a dry patch.
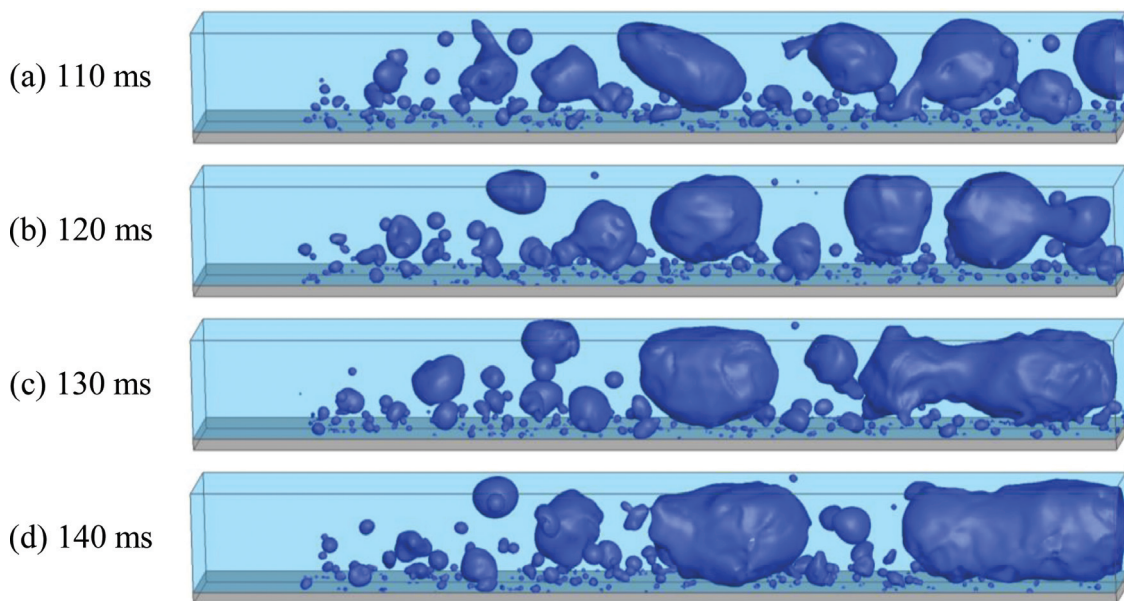
Fig. 18. Snapshots of 3D subcooled flow boiling in the mini-channel with a heat flux of 500 kW/m^2 from 110 to 140 ms.

4. Conclusions

In this paper, the conjugated heat transfer of 3D subcooled flow boiling in a rectangular mini-channel is investigated by the VOSET method in conjunction with a reasonable nucleation density site model. The simulation is conducted by a self-programming code. Within the studied heat flux range (100–500 kW/m^2), hundreds of bubbles are accurately captured, and different flow patterns are observed in the studied mini-channel. The heat transfer mechanisms under different heat fluxes are illustrated by the bubble activities, distributions of HTC, wall superheat, and vapor fraction. The major conclusions are summarized as follows.

(1) The flow pattern of subcooled flowing boiling in the mini-channel changes with heat flux. The pseudo bubbly flow, bubbly flow, slug flow, and pattern transition are predicted subsequently in the mini-channel with the increasing heat flux. A pseudo bubbly flow happens with a few activated bubble nucleation sites when the heat flux is low. As the increase of heat flux, more nucleation sites are activated, and the bubbly flow happens with the growth, coalescence, and detachment of many bubbles. Moreover, some elongated bubbles are formed and block the mini-channel with further increasing heat flux, and the transition from a bubbly flow to slug flow happens.

(2) The time-space average wall HTC increases firstly and then decreases with the heat fluxes. When the heat flux is below 400 kW/m^2, the nucleate boiling mainly dominates the heat transfer, which is enhanced by increasing heat flux. However, when the heat flux is raised to 500 kW/m^2, some big bubbles coalesce into an elongated bubble, and the liquid film below it dries out, leading to the formation of a dry patch on the heating wall. As a result, the heat transfer deteriorates rapidly, and HTC drops from the peak.

(3) The local time average HTC is related to the vapor fraction. The HTC changes slightly when the vapor fraction keeps at a low level. After the happening of bubbly flow, HTC increases with the increasing vapor fraction along the flow direction with a vapor fraction below 0.18. Furthermore, when the vapor fraction ranges from 0.18 to 0.45, HTC reaches a platform with a value of about 20,250 W/(m^2·K). However, HTC decreases with the further increase of vapor fraction (over 0.45) because of the formation of dry patches.

(4) The heat transfer mechanism of the subcooled boiling in the studied mini-channel includes both nucleate boiling dominance and convective boiling dominance. The nucleate boiling dominance is the primary heat transfer mechanism at a vapor fraction below 0.45, and the convective effect contributes to the HTC at a high vapor fraction before the formation of dry patches.

Declaration of Competing Interest

The authors declare that they have no known competing financial interests or personal relationships that could have appeared to influence the work reported in this paper.

CRediT authorship contribution statement

Yu-Jie Chen: Methodology, Data curation, Writing – original draft. **Kong Ling:** Data curation, Validation. **Hao Ding:** Writing – review & editing, Methodology, Investigation. **Yun Wang:** Investigation, Visualization. **Shu-Qi Jin:** Conceptualization, Visualization. **Wen-Quan Tao:** Methodology, Supervision, Conceptualization, Writing – review & editing.

References

[1] L. Cheng, G. Xia, Fundamental issues, mechanisms and models of flow boiling heat transfer in microscale channels, Int. J. Heat Mass Transf. 108 (2017) 97–127.

[2] I. Mudawar, Two-phase micro-channel heat sinks: theory, applications and limitations, J. Electron. Packag. 133 (4) (2011) 041002.

[3] P.E. Jimenez, I. Mudawar, A multi-kilowatt immersion-cooled standard electronic clamshell module for future aircraft avionics, J. Electron. Packag. 116 (3) (1994) 220–229.

[4] T.J. Laclair, I. Mudawar, Thermal transients in a capillary evaporator prior to the initiation of boiling, Int. J. Heat Mass Transf. 43 (21) (2000) 3937–3952.

[5] K.P. Drummond, D. Back, M.D. Sinanis, D.B. Janes, D. Peroulis, J.A. Weibel, S.V. Garimella, A hierarchical manifold microchannel heat sink array for high--heat-flux two-phase cooling of electronics, Int. J. Heat Mass Transf. 117 (2018) 319–330.

[6] I. Aranzabal, I.M.D. Alegria, N. Delmonte, P. Cova, I. Kortabarria, Comparison of the heat transfer capabilities of conventional single-phase and two-phase cooling systems for electric vehicle IGBT power module, IEEE Trans. Power Electron. 1 (2018) 4185–4194.

[7] J.R. Thome, State-of-the-art overview of boiling and two-phase flows in microchannels, Heat Transf. Eng. 27 (9) (2006) 4–19.

[8] S.S. Mehendale, A.M. Jacobi, R.K. Shah, Fluid flow and heat transfer at micro-and meso-scales with application to heat exchanger design, Appl. Mech. Rev. 53 (7) (2000) 175–193.

[9] N. Brauner, D.M. Maron, Identification of the range of 'small diameters' conduits, regarding two-phase flow pattern transitions, Int. Commun. Heat Mass Transf. 19 (1) (1992) 29–39.

[10] W. Qu, I. Mudawar, Flow boiling heat transfer in two-phase micro-channel heat sinks–-I. Experimental investigation and assessment of correlation methods, Int. J. Heat Mass Transf. 46 (15) (2003) 2755–2771.

[11] J. Lee, I. Mudawar, Fluid flow and heat transfer characteristics of low temperature two-phase micro-channel heat sinks–Part 1: experimental methods and flow visualization results, Int. J. Heat Mass Transf. 51 (17–18) (2008) 4315–4326.

[12] J. Lee, I. Mudawar, Fluid flow and heat transfer characteristics of low temperature two-phase micro-channel heat sinks–Part 2. Subcooled boiling pressure drop and heat transfer, Int. J. Heat Mass Transf. 51 (17–18) (2008) 4327–4341.

[13] J. Mathew, P.S. Lee, T. Wu, C.R. Yap, Experimental study of flow boiling in a hybrid microchannel-microgap heat sink, Int. J. Heat Mass Transf. 135 (2019) 1167–1191.

[14] Z.Y. Bao, D.F. Fletcher, B.S. Haynes, Flow boiling heat transfer of Freon R11 and HCFC123 in narrow passages, Int. J. Heat Mass Transf. 43 (18) (2000) 3347–3358.

[15] X. Huo, L. Chen, Y. Tian, T.G. Karayiannis, Flow boiling and flow regimes in small diameter tubes, Appl. Therm. Eng. 24 (8–9) (2004) 1225–1239.

[16] Y. Yan, T. Lin, Evaporation heat transfer and pressure drop of refrigerant R-134a in a small pipe, Int. J. Heat Mass Transf. 41 (24) (1998) 4183–4194.

[17] S. Lin, P.A. Kew, K. Cornwell, Flow boiling of refrigerant R141b in small tubes, Chem. Eng. Res. Des. 79 (4) (2001) 417–424.

[18] C.B. Tibirica, G. Ribatski, Flow boiling heat transfer of R134a and R245fa in a 2.3mm tube, Int. J. Heat Mass Transf. 53 (11–12) (2010) 2459–2468.

[19] S. Saitoh, H. Daiguji, E. Hihara, Effect of tube diameter on boiling heat transfer of R-134a in horizontal small-diameter tubes, Int. J. Heat Mass Transf. 48 (23–24) (2005) 4973–4984.

[20] X. Li, J. Xu, Nanofluid stabilizes and enhances convective boiling heat transfer in a single microchannel, Int. J. Heat Mass Transf. 55 (21–22) (2012) 5673–5686.

[21] A. Soleimani, A. Sattari, P. Hanafizadeh, Subcooled two-phase flow boiling in a microchannel heat sink: comparison of conventional numerical models, J. Comput. Appl. Mech. 51 (2020) 37–45.

[22] S. Osher, J.A. Sethian, Fronts propagating with curvature dependent speed: algorithms based on Hamilton-Jacobi formulations, J. Comput. Phys. 79 (1) (1988) 12–49.

[23] C.W. Hirt, B.D. Nichols, Volume of fluid (VOF) method for the dynamics of free boundary, J. Comput. Phys. 39 (1981) 201–225.

[24] M. Sussman, E.G. Puckett, A coupled level set and volume-of-fluid method for computing 3D and axisymmetric incompressible two-phase flows, J. Comput. Phys. 162 (2) (2000) 301–337.

[25] D. Sun, W. Tao, A coupled volume-of-fluid and level set (VOSET) method for computing incompressible two-phase flows, Int. J. Heat Mass Transf. 53 (4) (2010) 645–655.

[26] K. Ling, Z. Li, D. Sun, Y. He, W. Tao, A three-dimensional volume of fluid & l level set (VOSET) method for incompressible two-phase flow, Comput. Fluids 118 (2015) 293–304.

[27] K. Ling, S. Zhang, W. Liu, X. Sui, W. Tao, Interface tracking simulation for subcooled flow boiling using VOSET method, Front. Energy Res. 8 (2021) 526035.

[28] A. Mukherjee, S.G. Kandlikar, Numerical simulation of growth of a vapor bubble during flow boiling of water in a microchannel, Microfluid. Nanofluid. 1 (2) (2005) 137–145.

[29] A. Mukherjee, S.G. Kandlikar, Z.J. Edel, Numerical study of bubble growth and wall heat transfer during flow boiling in a microchannel, Int. J. Heat Mass Transf. 54 (15–16) (2011) 3702–3718.

[30] W. Lee, G. Son, Bubble dynamics and heat transfer during nucleate boiling in a microchannel, Numer. Heat Transf. Appl. 53 (10) (2008) 1074–1090.

[31] Y. Zu, Y. Yan, T.G. Karayiannis, D.B.R. Kenning, Confined bubble growth during flow boiling in a mini-/micro-channel of rectangular cross-section part II: approximate 3-D numerical simulation, Int. J. Therm. Sci. 50 (3) (2011) 267–273.

[32] J.R. Thome, M. Magnini, A CFD study of the parameters influencing heat transfer in microchannel slug flow boiling, Int. J. Therm. Sci. 110 (2016) 119–136.

[33] Y. Luo, W. Li, K. Zhou, K. Sheng, S. Shao, Z. Zhang, J. Du, W.J. Minkowycz, Three--dimensional numerical simulation of saturated annular flow boiling in a narrow rectangular microchannel, Int. J. Heat Mass Transf. 149 (2020) 110246.

[34] R. Zhuan, W. Wang, Flow pattern of boiling in micro-channel by numerical simulation, Int. J. Heat Mass Transf. 55 (5–6) (2012) 1741–1753.

[35] F. Huang, J. Zhao, Y. Zhang, H. Zhang, Z. Liu, Numerical analysis on flow pattern and heat transfer characteristics of flow boiling in the mini-channels, Numer. Heat Transf. Fundam. (2020) 1–27.

[36] Y.K. Prajapati, M. Pathak, M.K. Khan, Numerical investigation of subcooled flow boiling in segmented finned microchannels, Int. Commun. Heat and Mass Transf. 86 (2017) 215–221.

[37] G. Hedau, P. Dey, R. Raj, S.K. Saha, Experimental and numerical investigation of the effect of number of parallel microchannels on flow boiling heat transfer, Int. J. Heat Mass Transf. 158 (2020) 119973.

[38] J. Smagorinsky, General circulation experiments with the primitive equations, Mon. Weather Rev. 91 (1963) 89–96.

[39] M.M. Francois, S.J. Cummins, E.D. Dendy, D.B. Kothe, J.M. Sicilian, M.W. Williams, A balanced-force algorithm for continuous and sharp interfacial surface tension models within a volume tracking framework, J. Comput. Phys. 213 (1) (2006) 141–173.

[40] K. Ling, G. Son, D. Sun, W. Tao, Three dimensional numerical simulation on bubble growth and merger in microchannel boiling flow, Int. J. Therm. Sci. 98 (2015) 150–163.

[41] Y. Luo, W. Li, K. Zhou, K. Sheng, S. Shao, Z. Zhang, J. Du, W.J. Minkowycz, Three--dimensional numerical simulation of saturated annular flow boiling in a narrow rectangular microchannel, Int. J. Heat Mass Transf. 149 (2020) 119246.

[42] F. Huang, J. Zhao, Y. Zhang, H. Zhang, C. Wang, Z. Liu, Numerical analysis on flow pattern and heat transfer characteristics of flow boiling in the mini-channels, Numer. Heat Transf. Part B Fundam. 78 (4) (2020) 221–247.

[43] A. Urbano, S. Tanguy, G. Huber, C. Colin, Direct numerical simulation of nucleate boiling in micro-layer regime, Int. J. Heat Mass Transf. 123 (2018) 1128–1137.

[44] Q. Li, Y. Jiao, M. Avramova, P. Chen, J. Yu, J. Chen, J. Hou, Development, verification and application of a new model for active nucleation site density in boiling systems, Nucl. Eng. Des. 328 (2018) 1–9.

[45] K.E. Gungor, R.H.S. Winterton, General correlation for flow boiling in tubes and annuli, Int. J. Heat Mass Transf. 26 (1986) 351–358.

[46] T.L. Bergman, A.S. Lavine, F.P. Incropera, D.P. DeWitt, in: Introduction to Heat Transfer, 516, 6th ed., John Wiley & Sons, Inc., New York, 2011, p. 628. Pages.

[47] M.G. Cooper, Heat flow rates in saturated nucleate pool boiling–a wide ranging examination using reduced properties, Adv. Heat Transf. 16 (1984) 157–239.

[48] Y.A. Cengel, in: Heat and Mass Transfer:a Practical Approach, 3rd Ed., McGraw-Hill, Boston, 2007, p. 569. Pages.

[49] R. Situ, T. Hibiki, M. Ishii, M. Mori, Bubble lift-off size in forced convective subcooled boiling flow, Int. J. Heat Mass Transf. 48 (25) (2005) 5536–5548.